PAPER

Journal of Materials Chemistry C Accepted Manuscript

SiTe Monolayers: Si-Based Analogues of Phosphorene

Yu Chen, [a] Qiang Sun, *[abc] and Puru Jena [c]

Complementing the group of two-dimensional (2D) binary phosphorene analogues, we carried out first-principles calculations for α-SiTe and β-SiTe monolayers which are respectively black-phosphorene-like and blue-phosphorene-like. We show that both of the SiTe monolayers are dynamically, thermally and mechanically stable, although α-SiTe with significant elastic anisotropy is energetically more favorable than β-SiTe. Both monolayers exhibit superior mechanical flexibility and are indirect-gap semiconductors with band gaps of 0.57 and 2.36 eV, respectively. What is even more important is that α-SiTe monolayer can be tuned from an indirect band gap semiconductor to a direct band gap semiconductor and eventually to a metal when biaxial strains are applied, showing a high degree of flexibility in band engineering which is absent in non-silicon based analogues.

Introduction

Recently, considerable efforts have been made to explore properties of 2D group V materials such as phosphorene, arsenene, and antimonene. Because of their unique structures and novel properties, these materials have potential applications in flexible electronics, battery electrode devices, and optoelectronic devices. [1-5] Search for new 2D materials has recently been expanded to include the neighbors of group V elements, namely, IV-VI binary analogous sheets. So far, most of the studies involve Ge-based and Sn-based monolayers such as GeS, GeSe, SnS, and SnSe, etc. For example, Ulaganathan *et al*. reported GeS nanosheet-based field-effect transistors with high photocurrent generation, broad spectral range, and long-term stability, which are promising for future optoelectronic applications. [6] Tan *et al*. studied the electrochemical properties of layered GeS for catalytic applications. [7] Hu *et al*. found that the distorted NaCl-type GeSe monolayer is a semiconductor with tunable direct band gap and small carrier effective mass. [8] Ramasamy *et al*. have synthesized 2D nanosheets of GeS and GeSe for high-sensitivity photodetectors. [9] Shi *et al*. theoretically predicted that single-layer and double-layer SnSe and GeSe are promising materials for ultrathin-film photovoltaic applications. [10] Tritsaris *et al*. studied the opto-electronic properties of SnS as a function of number of layers and found that SnS is non-toxic and can be used for high efficiency photovoltaic cells. [11] Li *et al*. and Ma *et*

al. have recently synthesized 2D nanosheets of SnSe. [12, 13] Currently, the most important finding in SnSe is that both the bulk and single-layered materials display high thermoelectric efficiencies with great potential for conversion of heat to electricity. [14-16] Gomes *et al*. theoretically analyzed their electronic, optical, and piezoelectric properties. [17, 18] Fei *et al*. predicted that these 2D structures with giant piezoelectric effects may be promising candidates for piezoelectric applications. [19] Arunima *et al*. studied this family of group-IV monochalcogenides for optoelectronics and solar energy conversion. [20]

Compared to the widely studied silicene [21-23] which has no band gap in its pristine form, the advantage of a Si based binary sheet is that it has a finite band gap which is required for application in switching devices. In fact, very few studies are available on Si-based binary systems. Recently, Zhu *et al*. studied isoelectronic counterparts of group V semiconductors such as silicon monosulfide and SiS-P heterostructures for potential electronic applications. [24] Due to the compatibility with the well-developed Si-based semiconductor industry, it is useful to extend these studies to the Si-based phosphorene-like monolayered materials. In spite of the merit of Si-based monochalcogenide materials, a systematic study of 2D silicon monotelluride monolayers is lacking. Note that Si_2Te_3 was considered as the only crystal in the silicon-tellurium series. [25] However, research can make it possible to break the traditional barrier in search of unexpected materials. Therefore, in this work, we use first-principles calculations to systematically investigate the structures, stability, mechanical, and electronic properties of previously unknown silicon monotelluride monolayers and explore how strain can be used to modulate their band-gaps. We also compare the properties of two SiTe monolayers with other analogous materials to highlight the merits of Si-based materials.

[a.] *Department of Materials Science and Engineering, Peking University, Beijing 100871, China. Email: sunqiang@pku.edu.cn*

[b.] *Center for Applied Physics and Technology, Peking University, Beijing 100871, China*

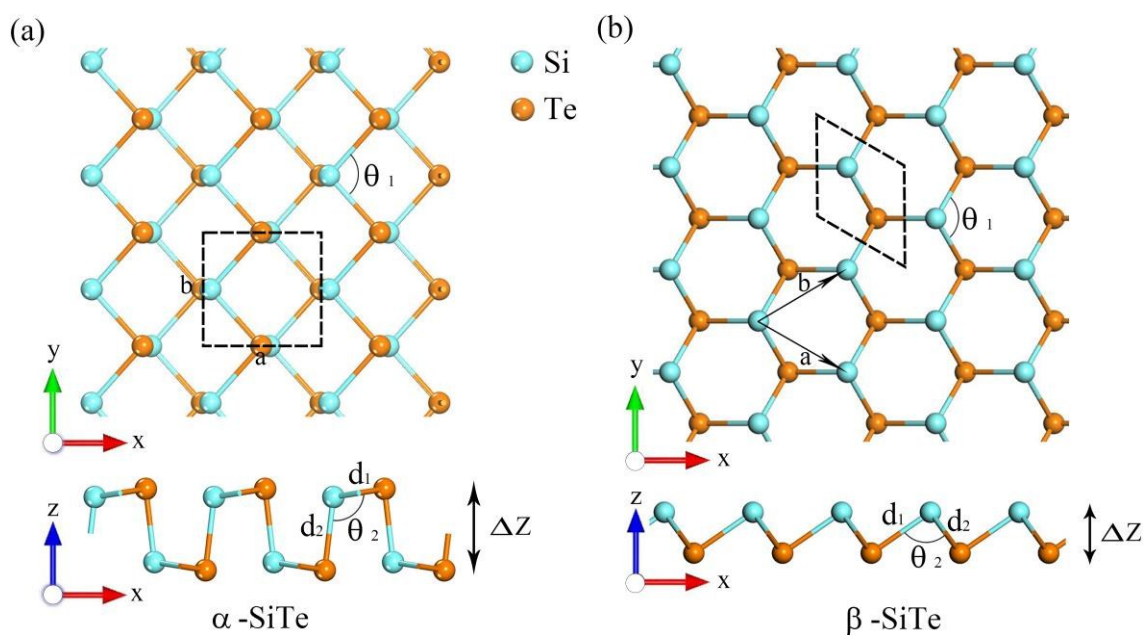[c.] *Department of Physics, Virginia Commonwealth University, Richmond, VA 23284, USA*

This journal is © The Royal Society of Chemistry 2016

J. Mater. Chem. C, 2016, **00**, 1-3 | **1**

Fig. 1 Geometric structures of 2D silicon-telluride monolayers. The top view and side view of (a) α-SiTe and (b) β-SiTe monolayers. The unit cell is marked with a dashed box and rhombus for α-SiTe and β-SiTe, respectively.

Table 1 Structural and electronic properties of 2D α-SiTe and β-SiTe. Shown are the lattice parameters (Å) a_1 and a_2, and the out of plane displacements (Å) Δz, the bond lengths (Å) and angles (°), the space group, the cohesive energy (eV/atom), E_c, and the formation energy, E_f (meV), energy band gaps (eV) calculated using the PBE functional, E_g (PBE) and HSE06 functional, E_g (HSE), and the charge transfer (e) from Si atom to Te atom, T_B, calculated using the Bader formalism in units of the elementary charge.

	a	b	Δz	d_1	d_2	θ_1	θ_2	Symmetry	E_C	E_f	E_g (PBE)	E_g (HSE)	T_B
α-SiTe	4.29	4.11	2.92	2.78	2.64	95.6	100.5	$Pmn2_1$ 31	3.30	32.4	0.40	0.57	0.36
β-SiTe	3.83	3.83	1.53	2.69	2.69	90.9	90.9	$P3m1$ 156	3.27	61.6	1.83	2.36	0.40

Computational methods

Calculations are based on density functional theory (DFT) and carried out using the Vienna ab initio Simulation Package (VASP) [26]. The electron-ion interaction is treated by projector-augmented-wave (PAW) potentials [27]. Exchange-correlation functional is taken into account using the Perdew-Burke-Ernzerhof (PBE) form of the generalized gradient approximation. Hybrid Heyd-Scuseria-Ernzerhof (HSE06) functional [28] is used to achieve better accuracy of the electronic and optical absorption properties. To estimate total electronic charge of atoms, Bader charge analysis [29] are performed using the code developed by Henkelman's group [30-32]. The energy cutoff is set to 520 eV and the total energy and force are converged to 1×10^{-7} eV and 1×10^{-5} eV/Å, respectively. The Brillouin zone is represented with (19 × 19 × 1) Monkhorst-Pack special k-point meshes [33]. For calculations on the 2D systems, a vacuum space of ~20 Å along the z direction is applied to avoid interactions between two neighbor images. All the structures are fully relaxed using conjugated gradient scheme without any symmetric constraints. To confirm their dynamic stability, phonon calculations were performed using finite displacement method as implemented in the Phonopy program [34].

Results and discussion

The geometric structures of 2D SiTe monolayers are given in Fig. 1. Since each Si atom is covalently bonded to three Te atoms, resulting in a hexagonal unit cell, the buckling occurs at various points in the unit cell. This gives rise to two different types of lattice arrangements. For convenience of discussion, we term the two structures as α-SiTe and β-SiTe, respectively. One can see that the isotropic structure of β-SiTe in Fig. 1b differs significantly from the anisotropic structure of α-SiTe in Fig. 1a. Orthorhombic monolayer α-SiTe belongs to space group of Pmn21 (No. 31). The optimized lattice parameters, namely, a = 4.29 Å and b = 4.11 Å. are about 3% and 7% smaller than the lattice constants of α-GeTe and α-SnTe monolayers [20], respectively. Compared to the previously studied α-SiS monolayer [24], Te atoms in α-SiTe are located more outwardly on the layer than S, due to the larger atomic size of Te. As shown in Fig. 1b, β-SiTe monolayer is a puckered honeycomb structure with a higher symmetry space group of P3m1 (No. 156). The corresponding lattice constants are a = b = 3.83 Å, which are about 12% and 14% longer than those of silicon monosulfide and blue phosphorene. The buckling parameters Δz, defined as the vertical distance separating the two atomic planes in these structures, are found to be 2.92
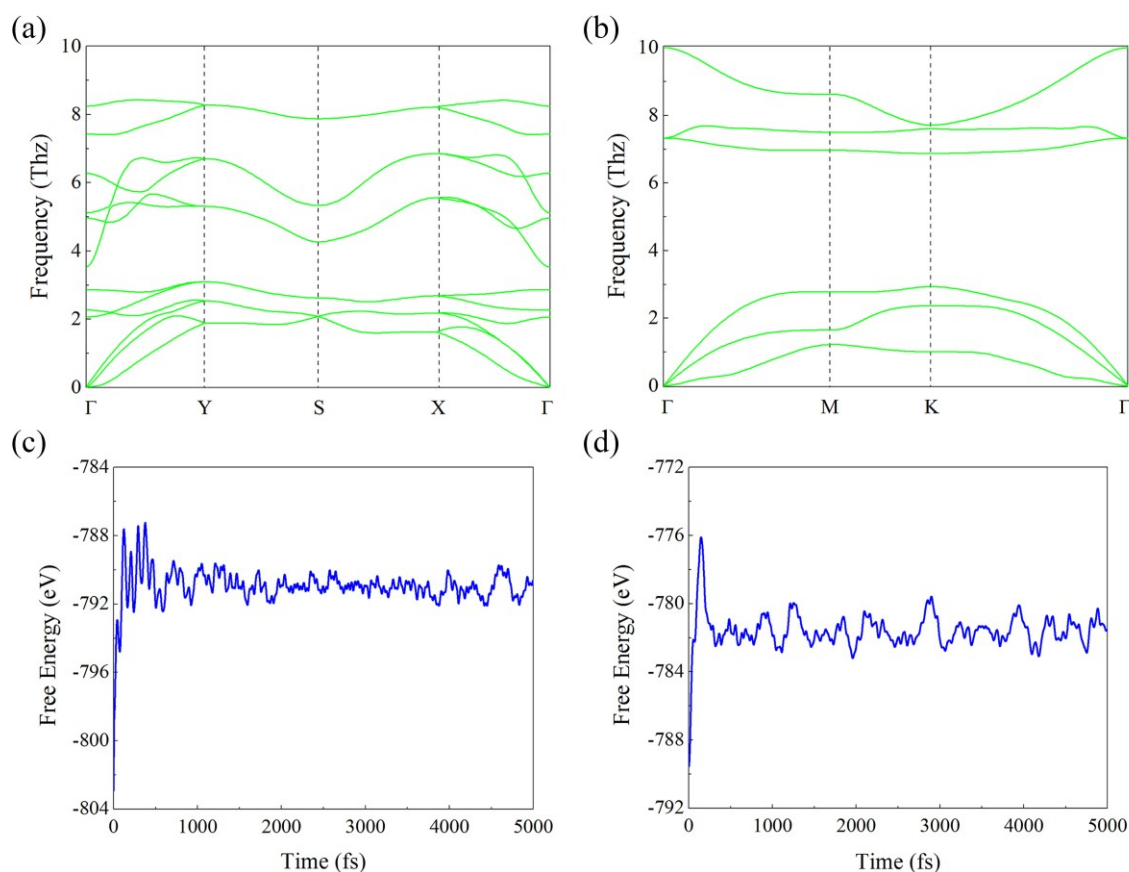
2 | *J. Mater. Chem. C*, 2016, **00**, 1-3

This journal is © The Royal Society of Chemistry 2016

Paper

Fig. 2 (a) and (b) Phonon dispersions of α-SiTe and β-SiTe along the high symmetric k-point path in the first Brillouin zone, respectively. The high symmetry k points are: Γ (0, 0, 0), Y (-1/2, 0, 0), S (-1/2, 1/2, 0), and X (0, 1/2, 0) for α-SiTe, and Γ (0, 0, 0), M (0, 1/2, 0), K (-1/3, 2/3, 0) for β-SiTe, respectively. (c) and (d) Energy fluctuation of α-SiTe and β-SiTe, respectively, with respect to time in AIMD simulations at 300 K.

and 1.53 Å for α-SiTe and β-SiTe monolayers, respectively. We calculated the cohesive energy, E_C, by using the equation E_C = -[E(SiTe) - nE(Si) - nE(Te)]/2n. Here E(SiTe) stands for the energy of SiTe per unit cell, n is the number of Si (Te) atoms per unit cell, and E(Si) and E(Te) are the energies of free Si and Te atoms. As can be seen in Table 1, the calculated binding energies are 3.30 and 3.27 eV per atom, indicating relatively strong binding in both the materials, with α-SiTe being energetically more stable. We further calculated the formation energy defined as E_f = [E(SiTe)$_{2D}$ - nE(Si)$_{3D}$ - nE(Te)$_{3D}$]/2n, where E_{2D} and E_{3D} are the energies of the monolayer and bulk materials, respectively, and n denotes the number of Si (Te) atoms in the respective unit cells. The calculated formation energies are about 32 and 62 meV/atom for α-SiTe and β-SiTe monolayers, respectively. Thus, the low formation energies of both the two sheets indicate that they could be extracted as free-standing or suspended single-layer flakes. [35] Since α-SiTe monolayer is the more stable phase in energy and has a lower formation energy, thus we predict that α-SiTe monolayer may be a more promising structure to be fabricated in experiment.

To confirm the dynamical stability phonon dispersions of silicon-telluride monolayers are calculated by using the finite displacement method. The results are plotted in Fig. 2a and 2b for α-SiTe and β-SiTe, respectively. We see that there is no

appreciable imaginary vibrational frequency in the first Brillouin zone, which clearly suggests that both α and β phases of SiTe monolayers are dynamically stable.

To further examine their thermal stability at finite-temperatures, we performed ab initio molecular dynamics (AIMD) simulations by using canonical (NVT) ensemble. The (7 × 7 × 1) and (10 × 10 × 1) supercells are used respectively for α-SiTe and β-SiTe monolayers to minimize the constraint induced by periodicity. The simulations are carried out with a Nosé thermostat at 300 K for 5 picoseconds with a time step of 1 femtosecond. The fluctuation of total energy with simulation time is plotted in Fig. 2c and 2d for α-SiTe and β-SiTe, respectively. The snapshots of atomic configurations of α- and β-SiTe monolayers in the AIMD simulations are shown in Fig. S1 (ESI†). After 5000 steps, we found no obvious distortion of the geometries and the total energies remain almost invariant during the entire simulation for both α-SiTe and β-SiTe monolayers. This confirms that structures are thermally stable at room temperature.

The mechanical stability of these materials is studied by calculating the linear elastic constants which in turn are calculated from the total energy as a function of small strains ε around the equilibrium positions. In the linear elastic range the elastic constant tensor C_{ij} forms a symmetric (6 × 6) matrix
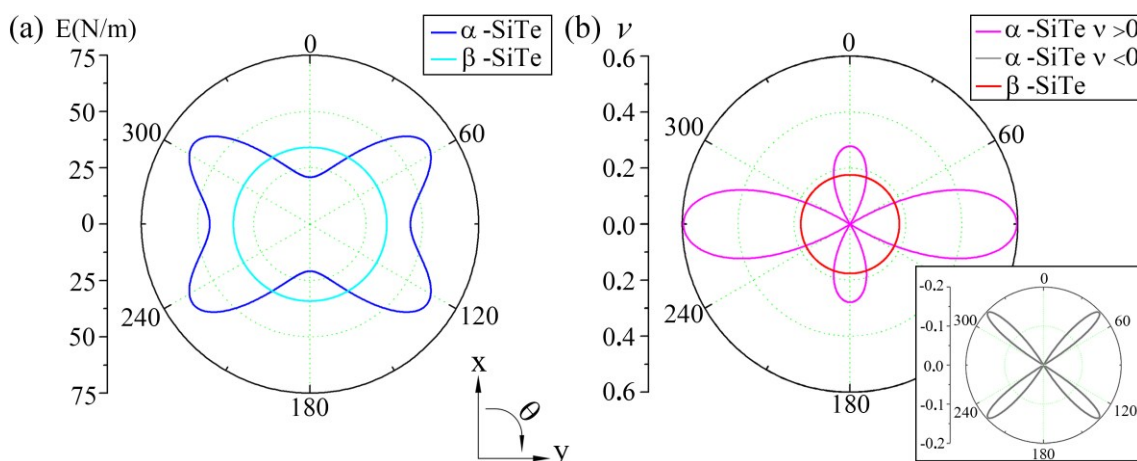
Fig. 3 Polar diagram for (a) Young's modulus E (N/m) and (b) Poisson's ratio *v* of α-SiTe and β-SiTe monolayers. The inset shows negative Poisson's ratio of β-SiTe monolayer. The angle θ identifies extension direction with respect to the x direction in the unit cell.

Table 2 Effective independent elastic constants (C_{ij}, N·m^{-1}), Young's modulus (E, N·m^{-1}) and Poisson's ratio (v) of α-SiTe and β-SiTe monolayers.

	C_{11}	C_{22}	C_{12}	C_{44}	E	v
α-SiTe	25.0	53.5	14.9	33.8	20.8~62.9	-0.20~0.60
β-SiTe	35.2	35.2	6.2	14.5	34.1	0.18

with 21 independent components. The elastic constants of 2D structures [36] are given in units of N·m^{-1}. Due to the symmetry of these materials, there are four and three independent elastic constants for 2D orthorhombic and hexagonal crystals, respectively, namely C_{11}, C_{22}, C_{12}, C_{44} and C_{11}, C_{12}, C_{44} (C_{11} = C_{22}). Thus, the mechanical stability of α-SiTe monolayer should satisfy the Born criteria [37], namely

$$(C_{11} + C_{22} - 2C_{12}) > 0,$$
$$C_{11} > 0, C_{22} > 0, C_{44} > 0,$$
$$(C_{11} + C_{22} + 2C_{12}) > 0,$$

and corresponding mechanical stability conditions for β-SiTe monolayer are

$$C_{11} > 0, C_{44} > 0,$$
$$C_{11} - C_{12} > 0.$$

To realize potential applications of these materials for flexible electronic devices, a thorough knowledge of their mechanical properties is required. Since the in-plane stiffness of graphene is well studied, we further plot the polar diagrams of Young's modulus $E(\theta)$ and Poisson's ratio $v(\theta)$ along an arbitrary direction θ as [38]:

$$E(\theta) = \frac{C_{11}C_{22} - C_{12}^2}{C_{11}s^4 + C_{22}c^4 + (\frac{C_{11}C_{22} - C_{12}^2}{C_{44}} - 2C_{12})c^2s^2},$$

$$v(\theta) = \frac{(C_{11} + C_{22} - \frac{C_{11}C_{22} - C_{12}^2}{C_{44}})c^2s^2 - C_{12}(c^4 + s^4)}{C_{11}s^4 + C_{22}c^4 + (\frac{C_{11}C_{22} - C_{12}^2}{C_{44}} - 2C_{12})c^2s^2},$$

where *c = cos θ* and *s = sin θ*.

Similar to single-layered black phosphorus, α-SiTe monolayer exhibits an anisotropic mechanical behavior due to its orthorhombic symmetry. The resulting Young's modulus and Poisson's ratio of α-SiTe monolayer depend sensitively on the direction. As shown in Fig. 3a, one can see that the Young's modulus of α-SiTe in the y direction is 2 times larger than its counterpart in the x direction and the maximum occurs along the diagonal direction with the value of 63 N/m. For an isotropic system, the maximum Poisson's ratio is up to 0.5 for the perfect incompressible material [39]. However, in an anisotropic orthorhombic system, the Poisson's ratio exceeds 0.5 along certain directions due to the large difference between C_{11} and C_{22}. We find that the α-SiTe monolayer has $v(\theta)$ up to 0.6 along the y direction, implying harder compression along these special directions. Interestingly, an unconventional negative Poisson's ratio is found along some directions in α-SiTe monolayer as shown in Fig. 3b. This means that when the monolayer is stretched longitudinally, it will shorten laterally. We find the value to be larger than that in single-layer black phosphorus [40]. So far, there is no complete theory to explain the mechanism of negative Poisson's ratio, but the hinged atomic structure may play an important role in this phenomenon. For hexagonal β-SiTe monolayer with trigonal symmetry, the isotropic elasticity of the system leads to $C_{11} = C_{22}$, and $C_{44} = (C_{11} - C_{12})/2$ and a perfect circular shape of the $E(\theta)$ and $v(\theta)$ can be seen in Fig. 3. The Young's moduli are 34 N/m in all directions and Poisson's ratio, namely C_{12}/C_{11} is 0.18. Compared to other 2D materials, such as graphene and MoS$_2$, SiTe monolayers are more flexible with a much smaller Young's modulus. Due to their isostructural nature this result is consistent with single-layer black phosphorus and blue phosphorus. We believe that the smaller Young's modulus in these materials may be resulting from the weaker Si-Te bond strength and the compromised dihedral angles, rather than bond length stretch when strain is applied. The increased flexible nature of the materials makes them a good choice for practical large magnitude in-plane strain engineering.
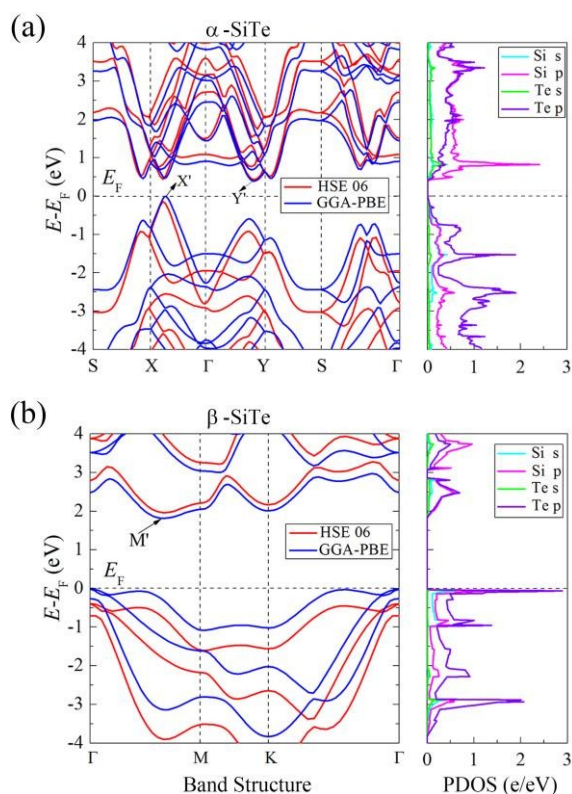
4 | *J. Mater. Chem. C*, 2016, **00**, 1-3

This journal is © The Royal Society of Chemistry 2016

Journal of Materials Chemistry C   **Paper**

Fig. 4 Calculated band structures and corresponding partial DOS of (a) α-SiTe and (b) β-SiTe monolayers with red and blue lines representing results using GGA-PBE and HSE06 functionals, respectively.

Fig. 5 (a) The dependence of the energy per atom on biaxial strain in α-SiTe and β-SiTe monolayers. Inset shows schematic representations of α-SiTe and β-SiTe monolayers under biaxial strain. Electronic band gap of (b) α-SiTe and (c) β-SiTe monolayers as a function of the strain.

Using Bader charge analysis we estimate a net transfer from silicon to tellurium atoms of 0.36 electrons in α-SiTe and 0.40 electrons in β-SiTe. This transfer is consistent with the higher electronegativity of Te compared to that of the Si atom. We believed that geometric parameter is of vital importance to the electronic properties of the system. Since α-SiTe monolayer has two different Si-Te bond lengths (in Table 1), the average bond length $\tilde{d}$ is 2.73 Å, which is slightly larger than the Si-Te bond-length of 2.69 Å in β-SiTe monolayer. This may cause a smaller net charge transfer from Si to Te in α-SiTe than that in β-SiTe monolayer. To study the electronic properties of SiTe monolayers, we have calculated the electronic band structures of α-SiTe and β-SiTe monolayers. The results are shown in Fig. 4. Note that α-SiTe monolayer is an indirect band gap semiconductor with a band gap of 0.40 eV at the PBE level, as the valence band maximum (VBM) and conduction band minimum (CBM) are located at the X' point and the Y' point in the Brillouin zone, respectively. The value of 0.40 eV is much smaller than previously reported values for black-phosphorus-like single-layered counterparts such as phosphorene and the predicted α-SiS structure [1, 24]. Due to the anisotropy of the structure, the band structure also exhibits significant anisotropy compared to that along the Γ-X and Γ-Y directions near the top of the valence band. In analogy with phosphorene, α-SiTe should exhibit higher carrier mobility along the x-direction than along the y-direction. For β-SiTe
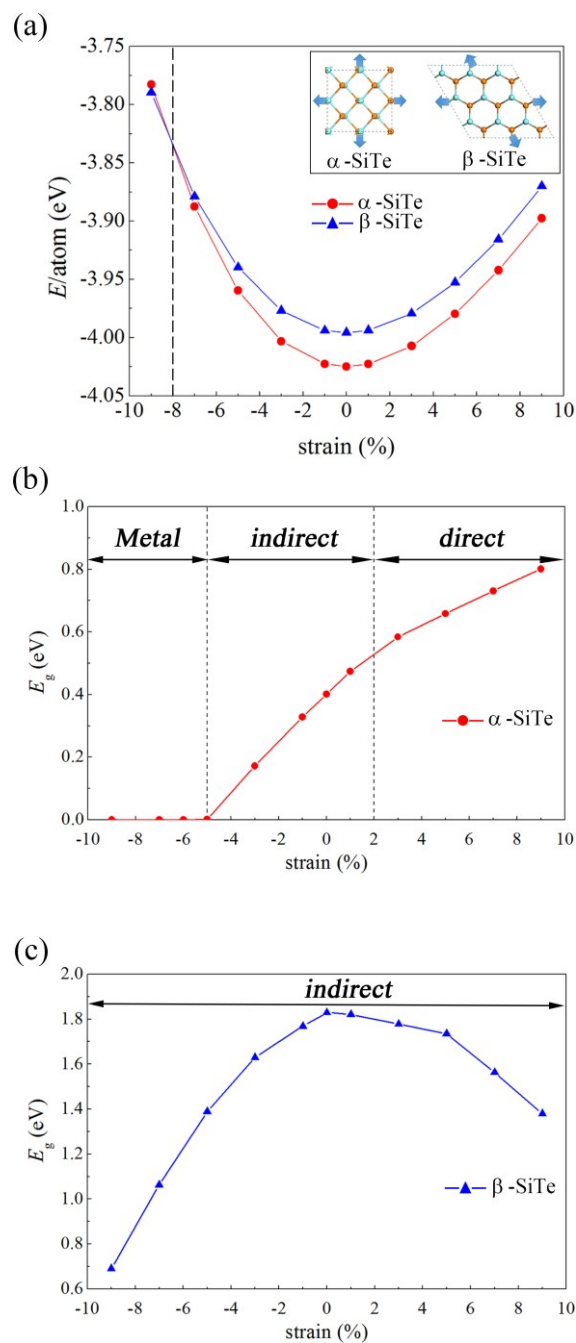
monolayer, the calculated band structure indicates that β-SiTe monolayer is a semiconductor with an indirect band gap of 1.83 eV at the PBE level, as the valence band maximum (VBM) and conduction band minimum (CBM) are located at the M' point and the Γ point in the Brillouin zone, respectively. We note that the top of the valence band is very flat, resulting in a heavy hole and a large density of states (DOS) in that region. As standard DFT calculations are known to significantly
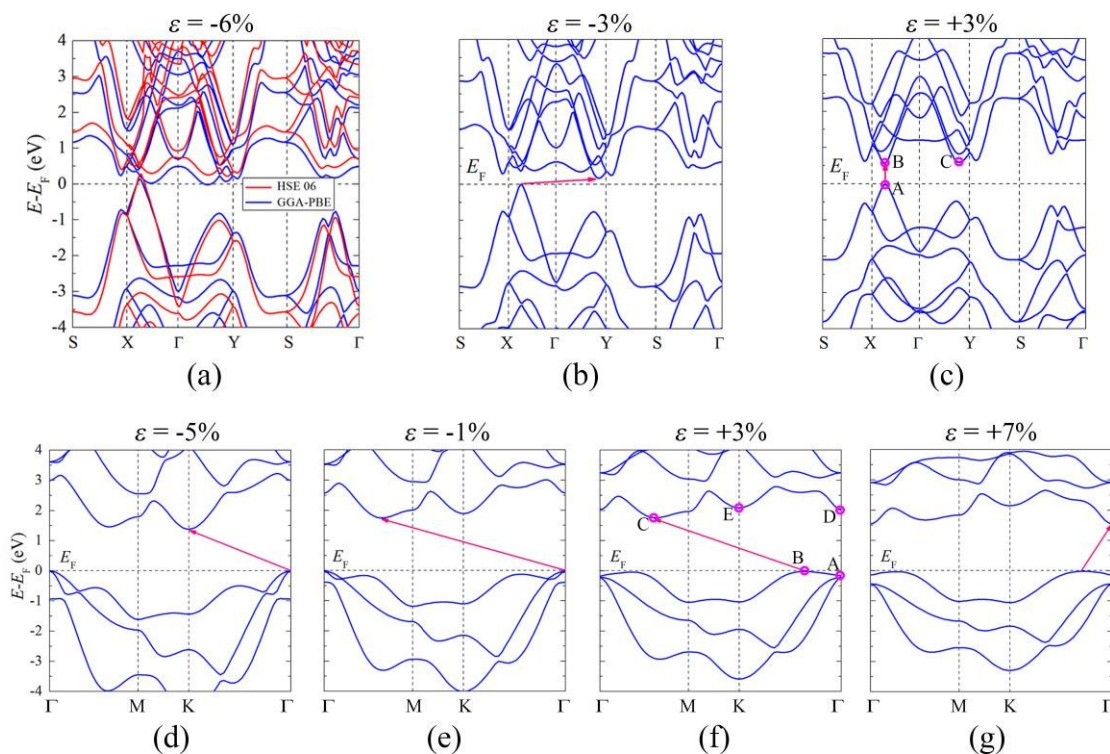
Fig. 6 (a - c) Electronic band structures of α-SiTe monolayer under -6% (a), -3% (b), and +3% (c) biaxial strain. (d - g) Electronic band structures of β-SiTe monolayer under a biaxial strain of -5% (d), -1% (e), +1% (f), and +7% (g). The near band edge states for α-SiTe and β-SiTe are labelled as (A, B, C) in (c) and (A, B, C, D, E) in (g) with pink circles, respectively.
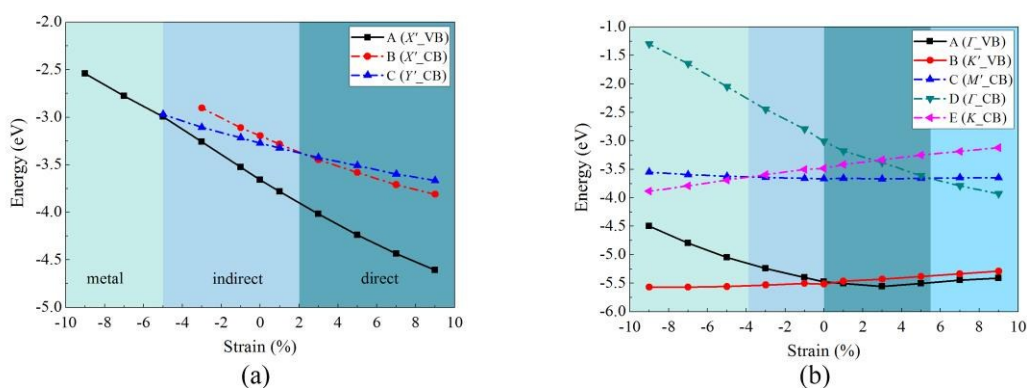

Fig. 7 Changes of energy of the near band edge states as a function of biaxial strain for (a) α-SiTe and (b) β-SiTe monolayers. All energies are relative to the vacuum level. The valence and conduction states are represented with solid, dash-dot lines, respectively.

underestimate the band gap, we repeated the band structure calculations using the screened hybrid functional HSE06 which has been demonstrated to be more accurate in describing the exchange-correction energy of electrons. The results are also plotted in Fig. 4 (red lines), showing that both the GGA and HSE06 functionals lead to similar dispersion curves of the valence and conduction bands. However, the conduction bands (CB) are up-shifted, while the valence bands (VB) are down-shifted at the HSE06 level, resulting in larger band gaps of 0.57 eV and 2.36 eV for monolayers of α-SiTe and β-SiTe, respectively. From the partial density of states (PDOS), one can

see that the VBM and CBM are mainly contributed by the Te p-electrons and Si p-electrons in α-SiTe, while both the VBM and CBM are mainly contributed by the p-electrons of Te and Si atoms, due to the large overlap in the PDOS of β-SiTe.

Recently, both experimental studies and theoretical calculations have shown that the band gaps can be tuned reversibly by applying elastic strain [41-44]. Here, we define the biaxial strain as $\varepsilon = (L - L_0)/L_0 \times 100\%$, where L_0 and L represent the lattice constants of SiTe monolayers in the equilibrium and strained states, respectively. We note that a low-dimensional material can in general sustain a larger strain without fracture

6 | *J. Mater. Chem. C*, 2016, **00**, 1-3

This journal is © The Royal Society of Chemistry 2016

Table 3 Changes of the VBM and CBM of α-SiTe monolayer with biaxial strain.
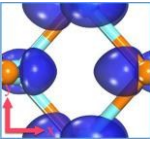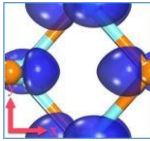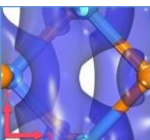
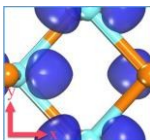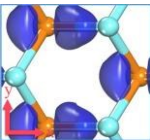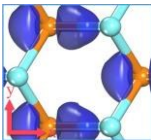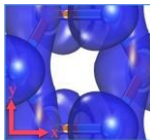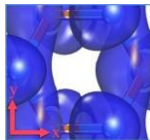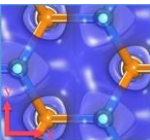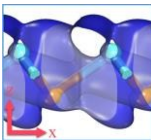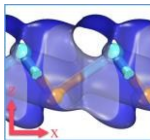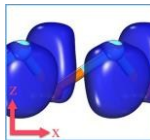|	Strain range	-9% ∼ -5%	-5% ∼ +2%	0 ∼ +2%
VBM	State	Metal	A	A
	Orbital component	—	Te: p_x Si: s	Te: p_x Si: s
	Electronic wave function	—		
CBM	State	—	C	B
	Orbital component	—	Si: p_x, p_y Te: p_x	Si: p_x Te: s
	Electronic wave function	—		

Table 4 Changes of the VBM and CBM of β-SiTe monolayer with biaxial strain.

	Strain range	-9% ∼ -4%	-4% ∼ 0	0 ∼ +5.5%	+5.5% ∼ +9%
VBM	State	A	A	B	B
	Orbital component	Te: p_x Si: p_x	Te: p_x Si: p_x	Te: p_z Si: p_z, s	Te: p_z Si: p_z, s
	Electronic wave function				
CBM	State	E	C	C	D
	Orbital component	Si: p_x, p_y Te: p_x, p_y	Si: p_z, p_x, s Te: p_z, p_x, s	Si: p_z, p_x, s Te: p_z, p_x, s	Te: p_z, s Si: p_z, s
	Electronic wave function				

than a bulk material. This property combined with the non-planarity of the structure of SiTe monolayers, allows us to simulate the effect of strain ε between -9% and +9%. The results are plotted in Fig. 5a. We see that α-SiTe is energetically more stable than β-SiTe in the range $-8\% < \varepsilon < +9\%$, while β-SiTe is more stable than α-SiTe when $\varepsilon < -8\%$. The typical E-ε curves indicate that both phases are stable. As seen in Fig. 5b and 5c, the fundamental band gap values of SiTe monolayers depend sensitively on the in-layer strain. To determine the critical strain of the electronic structure transition, we also plotted the energies of the near band edge states (labeled in Fig. 6) as a function of strain in Fig. 7a and 7b for α- and β-SiTe, respectively. As seen in Fig. 7, the energies of near band state almost linearly change with increasing of ε. Our results for α-SiTe in Fig. 5b indicate that the band gap

decreases when compressive strain is applied and increases when tensile strain is applied. Importantly, we find that α-SiTe monolayer experiences a metal-indirect-direct band-gap semiconductor transition at a relatively small critical strain. When $-5\% < \varepsilon < +2\%$, α-SiTe monolayers remain an indirect band-gap semiconductor, while it converts to a metallic phase with a compressive strain of $\varepsilon < -5\%$. Moreover, when tensile strain of $\varepsilon > +2\%$ is applied α-SiTe monolayer becomes a direct band-gap semiconductor, and such moderate tensile strain may possibly be induced by epitaxial mismatch with a substrate. For β-SiTe monolayer, a first general observation for the strained band structures is that the energy band gap reduces with increasing tensile and compressive strain, as illustrated in Fig. 5c while the indirect band-gap feature remains in the whole strain range. The largest change in the

band gap, namely, its reduction to 0.7 eV, may be achieved with a 9% compression. Within the ±9% range, we find that the band gap may be tuned in the range from ~0.7 to 1.8 eV, showing a flexible tunability of band gap.

To investigate the changes of the electronic properties of 2D-SiTe monolayers as a function of biaxial strain, we plotted the most significant variations of the band structure in Fig. 6, one can see that α-SiTe monolayer has three different electronic structures. For 0–5% compressive strain and 0–2% tensile strain, the VBM and CBM of α-SiTe monolayer remains between the X' and Y' points in the Brillouin zone (see Fig. 6b). However, further increase of the tensile strain up to about 2% shifts the CBM to the X' point, thus resulting in a direct band-gap semiconductor (see Fig. 6c), which remains for the tensile strain in the range of +2% to +9%. A progressive reduction of the energy band gap is then observed and it becomes zero when the compression reaches +5% (see Fig. 6a). The system then becomes metallic where the bottom of the conduction band and the top of the valence band at the X' point cross the Fermi level. Since GGA-PBE functional may incorrectly describe electronic structure, we repeated our calculation using HSE06 functional as shown in Fig. 6a (red line). The results suggest that the structure is indeed metallic, so α-SiTe monolayer could be very promising in various applications. It is noted that β-SiTe monolayer has no direct-indirect transition under biaxial strain but still shows electronic structure transitions at specified critical strain. As for the valence band states, VBM remains at the K' point when tensile strain is applied, but shifts to the Γ point when compressive strain is applied. On the other hand, the conduction band states have three different CBM states due to the band shifts. When $-4\% < \varepsilon < +5.5\%$, CBM remains at the M' point, while $\varepsilon < -4\%$ and $\varepsilon > +5.5\%$, the new CBM becomes at K point and Γ point, respectively. As shown in Fig. 6d-6g, β-SiTe monolayer has four different VBM-CBM configurations under strain, namely $\Gamma-K$, $\Gamma-M'$, $K'-M'$, and $K'-\Gamma$, respectively.

To better understand the changes in the band structure, the energies of near band edge states are explored by analyzing their decomposed charge distribution as well as their wave function character. The energy curves of near band edge state of α-SiTe monolayer are shown in Fig. 7a. Changes in the VBM and CBM and the corresponding electronic wave functions with biaxial strain are presented in Table 3. When strain is applied, different superposition of their atomic orbitals leads to the energy shifts of these states. In the applied strain range, the VBM of α-SiTe remains in A state, which is dominated by Te-5p_x orbitals mixed with Si-3s orbitals, having an anti-bonding like feature along the y direction. Thus, the increase of atomic distance can stabilize the orbitals and cause the energy to decrease. When $\varepsilon < -5\%$, the energy crossover of A and C state occurs, resulting in a metallic state. When $-5\% < \varepsilon < +2\%$, the CBM remains in C state, which consists of Si-3p_y and 3p_x orbitals and Te-5p_x orbitals, also resulting in an anti-bonding state. On the other hand, when $\varepsilon > +2\%$, B state becomes the CBM, which consists of Si-3p_x orbitals and Te-5s orbitals with bonding similar to that of A

state. Therefore, an indirect to direct band-gap transition occurs in the critical strain $\varepsilon = +2\%$.

Table 4 shows the changes of the VBM and CBM and the corresponding electronic wave functions of β-SiTe monolayer. The energy curves of near band edge state are shown in Fig. 7b. When $-9\% < \varepsilon < -4\%$, CBM is in the E-state, which is mainly described by the p_x and p_y orbitals of both Si and Te atoms forming a bonding-like state. The VBM remains in A state which is dominated by Te-5p_x orbitals mixed with Si-3p_x orbitals having an anti-bonding-like feature along the x direction. When $-4\% < \varepsilon < 0$, A state is still the VBM but C state emerges to the CBM composed by p_z, p_x and s orbitals of both Si and Te atoms, displaying bonding-like features along the x direction while anti-bonding like features along the y direction, and the competition of these two features makes the energy of C state being almost invariable. When the structure is stretched ($\varepsilon > 0$), B state becomes the VBM consisting of Si and Te p_z orbitals, bonded along the y direction and non-bonded along the x direction, resulting in a slight increase in energy. Meanwhile, the CBM is in C state for $0 < \varepsilon < +5.5\%$. The energy of D state becomes lower than that of C state when $\varepsilon > +5.5\%$, leading to a new CBM composed of the p_z orbitals of both Si and Te atoms showing an anti-bonding-like feature.

Conclusion

In summary, using first-principles density functional theory, we have performed extensive calculations to study the stability, mechanical and electronic properties of SiTe monolayers which are binary analogues of phosphorene. The effect of strain on the electronic structures of SiTe monolayers is also studied. We have identified two SiTe monolayers which are dynamically, thermally and mechanically stable. The α-SiTe monolayer is not only energetically more stable than β-SiTe monolayer, but also it can be changed from a semiconductor to a metal. The band gap can further be tuned form an indirect to a direct one. This high adjustability of band structures of the α-SiTe monolayer has not been observed either in black-phosphorene or in α-XTe (X=Ge, Sn) monolayers, showing the novelty in the Si-based analogue.

Acknowledgements

Notes and references

1.	H. Liu, A. T. Neal, Z. Zhu, Z. Luo, X. Xu, D. Tomanek and P. D. Ye, *ACS Nano*, 2014, **8**, 4033-4041.

2. Z. Zhu and D. Tomanek, *Phys Rev Lett*, 2014, **112**, 176802.
3. S. Zhang, Z. Yan, Y. Li, Z. Chen and H. Zeng, *Angew Chem Int Ed Engl*, 2015, **54**, 3112-3115.
4. G. Wang, R. Pandey and S. P. Karna, *ACS Appl Mater Interfaces*, 2015, **7**, 11490-11496.
5. A. S. Rodin, A. Carvalho and A. H. Castro Neto, *Phys Rev Lett*, 2014, **112**, 176801.
6. R. K. Ulaganathan, Y. Y. Lu, C. J. Kuo, S. R. Tamalampudi, R. Sankar, K. M. Boopathi, A. Anand, K. Yadav, R. J. Mathew, C. R. Liu, F. C. Chou and Y. T. Chen, *Nanoscale*, 2016, **8**, 2284-2292.
7. S. M. Tan, C. K. Chua, D. Sedmidubsky, Z. C. Sofer and M. Pumera, *Physical chemistry chemical physics : PCCP*, 2016, **18**, 1699-1711.
8. Y. Hu, S. Zhang, S. Sun, M. Xie, B. Cai and H. Zeng, *Applied Physics Letters*, 2015, **107**, 122107.
9. P. Ramasamy, D. Kwak, D.-H. Lim, H.-S. Ra and J.-S. Lee, *J. Mater. Chem. C*, 2016, **4**, 479-485.
10. G. Shi and E. Kioupakis, *Nano Lett*, 2015, **15**, 6926-6931.
11. G. A. Tritsaris, B. D. Malone and E. Kaxiras, *Journal of Applied Physics*, 2013, **113**, 8.
12. L. Li, Z. Chen, Y. Hu, X. Wang, T. Zhang, W. Chen and Q. Wang, *J Am Chem Soc*, 2013, **135**, 1213-1216.
13. X.-H. Ma, K.-H. Cho and Y.-M. Sung, *CrystEngComm*, 2014, **16**, 5080.
14. C. W. Li, J. Hong, A. F. May, D. Bansal, S. Chi, T. Hong, G. Ehlers and O. Delaire, *Nature Physics*, 2015, **11**, 1063-1069.
15. L. D. Zhao, G. Tan, S. Hao, J. He, Y. Pei, H. Chi, H. Wang, S. Gong, H. Xu, V. P. Dravid, C. Uher, G. J. Snyder, C. Wolverton and M. G. Kanatzidis, *Science*, 2016, **351**, 141-144.
16. F. Q. Wang, S. H. Zhang, J. B. Yu and Q. Wang, *Nanoscale*, 2015, **7**, 15962-15970.
17. L. C. Gomes and A. Carvalho, *Physical Review B*, 2015, **92**, 085406.
18. L. C. Gomes, A. Carvalho and A. H. Castro Neto, *Physical Review B*, 2015, **92**, 214103.
19. R. Fei, W. Li, J. Li and L. Yang, *Applied Physics Letters*, 2015, **107**, 173104.
20. A. K. Singh and R. G. Hennig, *Applied Physics Letters*, 2014, **105**, 042103.
21. S. Cahangirov, M. Topsakal, E. Akturk, H. Sahin and S. Ciraci, *Phys Rev Lett*, 2009, **102**, 236804.
22. Y. C. Cheng, Z. Y. Zhu and U. Schwingenschlögl, *EPL (Europhysics Letters)*, 2011, **95**, 17005.
23. T. P. Kaloni, Y. C. Cheng and U. Schwingenschlögl, *Journal of Applied Physics*, 2013, **113**, 104305.
24. Z. Zhu, J. Guan, D. Liu and D. Tomanek, *ACS Nano*, 2015, **9**, 8284-8290.
25. L. G. Bailey, *Journal of Physics and Chemistry of Solids*, 1966, **27**, 1593.
26. G. Kresse and J. Furthmuller, *Physical Review B*, 1996, **54**, 11169-11186.
27. G. Kresse and D. Joubert, *Physical Review B*, 1999, **59**, 1758-1775.
28. J. Heyd, G. E. Scuseria and M. Ernzerhof, *The Journal of Chemical Physics*, 2003, **118**, 8207.
29. R. F. W. Bader, *Chemical Reviews*, 1991, **91**, 893-928.
30. G. Henkelman, A. Arnaldsson and H. Jónsson, *Computational Materials Science*, 2006, **36**, 354-360.
31. E. Sanville, S. D. Kenny, R. Smith and G. Henkelman, *Journal of computational chemistry*, 2007, **28**, 899-908.
32. W. Tang, E. Sanville and G. Henkelman, *Journal of Physics: Condensed Matter*, 2009, **21**, 084204.
33. H. J. Monkhorst and J. D. Pack, *Physical Review B*, 1976, **13**, 5188-5192.
34. A. Togo, F. Oba and I. Tanaka, *Physical Review B*, 2008, **78**, 134106.
35. A. K. Singh, K. Mathew, H. L. Zhuang and R. G. Hennig, *J Phys Chem Lett*, 2015, **6**, 1087-1098.
36. C. Lee, X. Wei, J. W. Kysar and J. Hone, *Science*, 2008, **321**, 385-388.
37. O. Beckstein, J. E. Klepeis, G. L. W. Hart and O. Pankratov, *Physical Review B*, 2001, **63**, 134112.
38. E. Cadelano, P. L. Palla, S. Giordano and L. Colombo, *Physical Review B*, 2010, **82**, 235414.
39. H. Gercek, *International Journal of Rock Mechanics and Mining Sciences*, 2007, **44**, 1-13.
40. J. W. Jiang and H. S. Park, *Nat Commun*, 2014, **5**, 4727.
41. M. Huang, H. Yan, T. F. Heinz and J. Hone, *Nano Lett*, 2010, **10**, 4074-4079.
42. H. J. Conley, B. Wang, J. I. Ziegler, R. F. Haglund, Jr., S. T. Pantelides and K. I. Bolotin, *Nano Lett*, 2013, **13**, 3626-3630.
43. X. Peng, Q. Wei and A. Copple, *Physical Review B*, 2014, **90**, 085402.
44. Q. Wei and X. Peng, *Applied Physics Letters*, 2014, **104**, 251915.

TABLE OF CONTENTS (TOC)
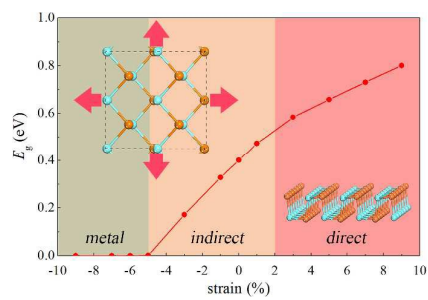
As a Si-based analogue of phosphorene, α-SiTe monolayer shows a high degree of flexibility in energy band engineering.